

Abstract

Measurement of total hadronic differential cross sections in the LArIAT experiment

Elena Gramellini

2018

6 Abstract goes here. Limit 750 words.

Measurement of total hadronic differential cross sections in the LArIAT experiment

A Dissertation
Presented to the Faculty of the Graduate School
of
Yale University
in Candidacy for the Degree of
Doctor of Philosophy

15 by
16 Elena Gramellini

¹⁷ Dissertation Director: Bonnie T. Fleming

18 Date you'll receive your degree

¹⁹

Copyright © 2017 by Elena Gramellini

²⁰

All rights reserved.

²¹ Contents

²² Acknowledgements	^{iv}
²³ 0 LArIAT: Liquid Argon In A Testbeam	¹
²⁴ 0.1 The Particles' Path to LArIAT	¹
²⁵ 0.2 LArIAT Tertiary Beam Instrumentation	⁴
²⁶ 0.2.1 Bending Magnets	⁴
²⁷ 0.2.2 Multi-Wire Proportional Chambers	⁶
²⁸ 0.2.3 Time-of-Flight System	⁸
²⁹ 0.2.4 Punch-Through and Muon Range Stack Instruments	⁹
³⁰ 0.2.5 LArIAT Cosmic Ray Paddle Detectors	¹¹
³¹ 0.3 In the Cryostat	¹²
³² 0.3.1 Cryogenics and Argon Purity	¹²
³³ 0.3.2 LArTPC: Charge Collection	¹⁵
³⁴ 0.3.3 LArTPC: Light Collection System	¹⁸
³⁵ 0.4 Trigger and DAQ	²⁰
³⁶ 0.5 Control Systems	²²
³⁷ A Measurement of LArIAT Electric Field	²⁸

³⁸ Acknowledgements

³⁹ A lot of people are awesome, especially you, since you probably agreed to read this
⁴⁰ when it was a draft.

⁴¹ Chapter 0

⁴² LArIAT: Liquid Argon In A

⁴³ Testbeam

⁴⁴ In this chapter, we describe the LArIAT experimental setup. We start by illustrating
⁴⁵ the journey of the charged particles in the Fermilab accelerator complex, from
⁴⁶ the gaseous thermal hydrogen at the Fermilab ion source to the delivery of the LAr-
⁴⁷ IAT tertiary beam at MC7. We then describe the LArIAT beamline detectors, the
⁴⁸ LArTPC, the DAQ and the monitoring system.

⁴⁹ 0.1 The Particles' Path to LArIAT

⁵⁰ LArIAT's particle history begins in the Fermilab accelerator complex with a beam of
⁵¹ protons. The process of proton acceleration develops in gradual stages (see picture
⁵² 1): gaseous hydrogen is ionized in order to form H^- ions; these ions are boosted to
⁵³ 750 keV by a Cockcroft-Walton accelerator and injected into the linear accelerator
⁵⁴ (Linac) that increases their energy up to 400 MeV; then, H^- ions pass through a
⁵⁵ carbon foil and lose the two electrons; the resulting protons are then injected into a
⁵⁶ rapid cycling synchrotron, called the Booster; at this stage, protons reach 8 GeV of
⁵⁷ energy and are compacted into bunches; the next stage of acceleration is the Main

58 Injector, a synchrotron which accelerates the bunches up to 120 GeV; in the Main
59 Injector, several bunches are merged into one and are ready for delivery.

60 The Fermilab accelerator complex works in supercycles of 60 seconds in duration.

61 A 120 GeV primary proton beam with variable intensity is extracted in four-second
62 “spills” and sent to the Meson Center beam line.

63 LArIAT’s home at Fermilab is the Fermilab Test Beam Facility (FTBF), where
64 the experiment characterizes a beam of charged particles in the Meson Center beam
65 line. At FTBF, the primary beam is focused onto a tungsten target to create LAr-
66 IAT’s secondary beam. The secondary beamline is set such that the composition of
67 the secondary particle beam is mainly positive pions. The momentum peak of the
68 secondary beam was fixed at 64 GeV/c for the LArIAT data considered in this work,
69 although the beam is tunable in momentum between 8-80 GeV/c; this configuration
70 of the secondary beamline assured a stable beam delivery at the LArIAT experimental
71 hall.

72 The secondary beam impinges then on a copper target within a steel collimator
73 inside the LArIAT experimental hall (MC7) to create the LArIAT tertiary beam,
74 (shown in Fig. 2). The steel collimator selects particles produced with a 13° pro-
75 duction angle. The particles are then bent by roughly 10° through a pair of dipole
76 magnets. By configuring the field intensity of the magnets we allow the particles of
77 LArIAT’s tertiary beam to span a momentum range from 0.2 to 1.4 GeV/c. The
78 polarity of the magnet is also configurable and determines the sign of the beamline
79 particles which are focused on the LArTPC. If the magnet polarity is positive the
80 tertiary beam composition is mostly pions and protons with a small fraction of elec-
81 trons, muons, and kaons. It is the job of the LArIAT beamline equipment to select the
82 particles polarity, to perform particle identification in the beamline and to measure
83 the momentum of the tertiary beam particles before they get to the LArTPC. The
84 LArIAT detectors are described in the following paragraphs.

Fermilab Accelerator Complex

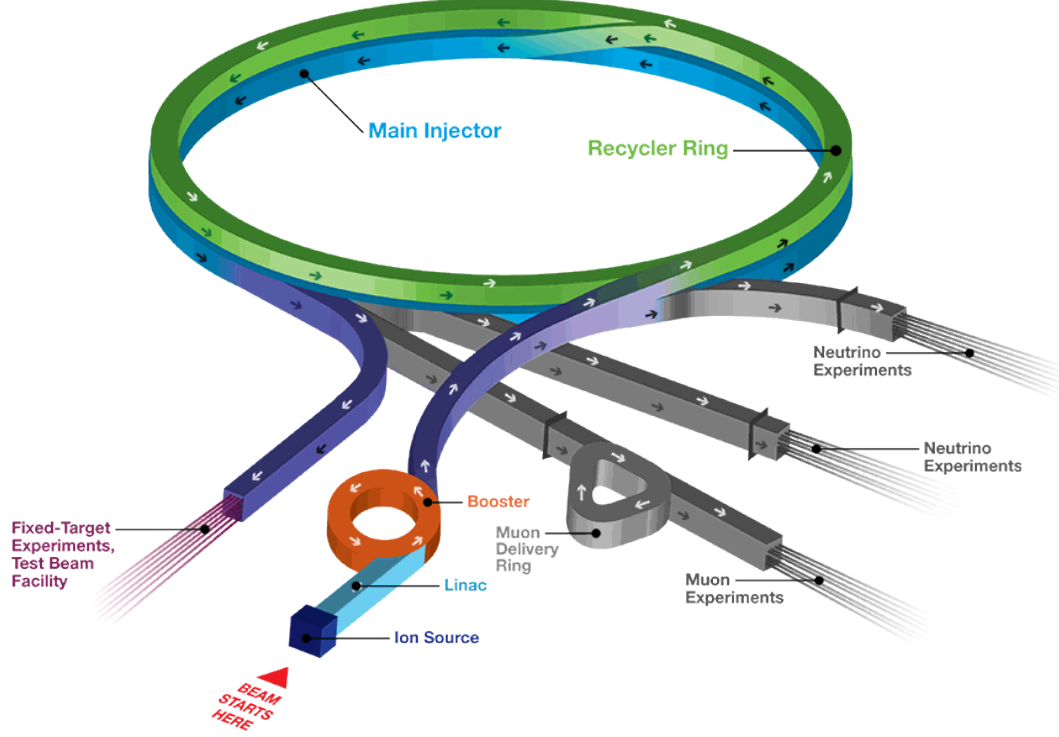


Figure 1: Layout of Fermilab Accelerator complex.

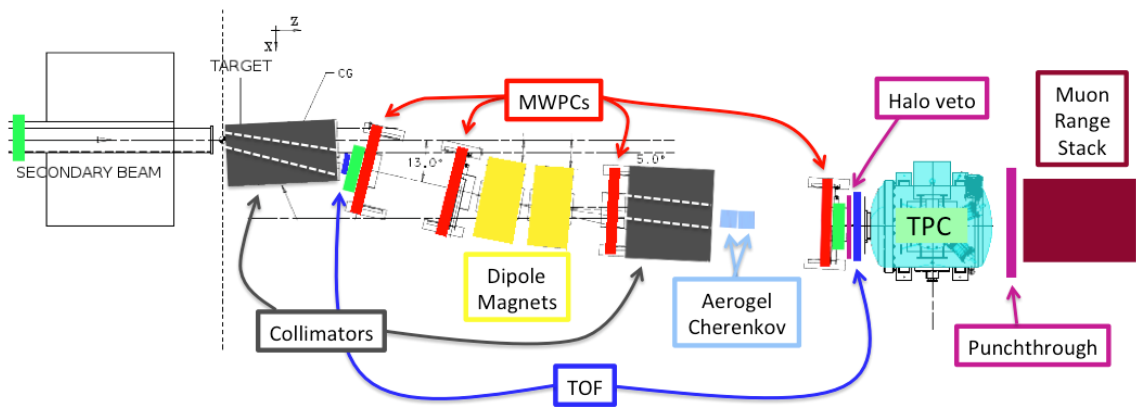


Figure 2: Bird's eye view of the LArIAT tertiary beamline. In grey: upstream and downstream collimators; in yellow: bending magnets; in red: multi wire proportional chambers; in blue: time of flight; in green: liquid argon TPC volume; in maroon: muon range stack.

85 0.2 LArIAT Tertiary Beam Instrumentation

86 The instrumentation of LArIAT tertiary beam and the TPC components have changed
87 several times during the three years of LArIAT data taking. The following paragraphs
88 describe the components operational during “Run II”, the data taking period relevant
89 to the hadron cross section measurements considered in this thesis.

90 The key components of the tertiary beamline instrumentation for the hadron cross
91 section analyses are the two bending magnets, a set of four wire chambers (WCs)
92 and two time-of-flight scintillating paddles (TOF) and, of course, the LArTPC. The
93 magnets determine the polarity of the particles in the tertiary beam; the combination
94 of magnets and wire chambers determines the particles’ momenta, which is used to
95 determine the particle species in conjunction with the TOF. A muon range stack
96 downstream from the TPC and two sets of cosmic paddles configured as a telescope
97 surrounding the TPC are also used for calibration purposes. A couple of Aerogel
98 Cherenkov counters, which we will not describe here as they are not used in the
99 hadron cross section measurements, completes the beamline instrumentation.

100 0.2.1 Bending Magnets

101 LArIAT uses a pair of identical Fermilab type “NDB” electromagnets, recycled from
102 the Tevatron’s anti-proton ring, in a similar configuration used for the MINERvA
103 T-977 test beam calibration [8]. The magnets are a fundamental piece of the LArIAT
104 beamline equipment, as they are used for the selection of the particle polarity and
105 for the momentum measurement before the LArTPC. The sign of the current in the
106 magnets allows us to select either positively or negatively charged particles; the value
107 of the magnetic field is used in the momentum determination and in the subsequent
108 particle identification.

109 We describe here the characteristics and response of one magnet, as the second one

110 has a similar response, given its identical shape and history. Each magnet is a box with
 111 a rectangular aperture gap in the center to allow for the particle passage. The magnet
 112 aperture measures 14.22 cm in height, 31.75 cm in width, and 46.67 cm in length.
 113 Since the wire chambers aperture (~ 12.8 cm 2) is smaller than the magnet aperture,
 114 only the central part of the magnet gap is utilized. The field is extremely uniform
 115 over this limited aperture and was measured with two hall probes, both calibrated
 116 with nuclear magnetic resonance probes. The probes measured the excitation curve
 117 shown in Figure 3.

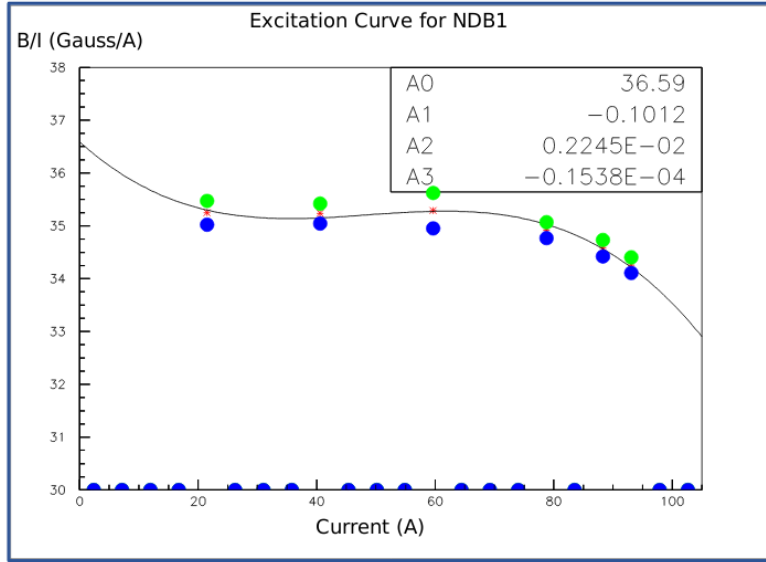


Figure 3: Magnetic field over current as a function of the current, for one NDB magnet (excitation curve). The data was collected using two hall probes (blue and green). We fit the readings with a cubic function (black) to average of measurements (red) given in the legend [7].

118 The current through the magnets at a given time is identical in both magnets.
 119 For the Run II data taking period, the current settings explored were 60A ($B \sim 0.21$
 120 T) and 100A ($B \sim 0.35$ T) in both polarities. Albeit advantageous to enrich the
 121 tertiary beam composition with high mass particles such as kaons, we never pushed
 122 the magnets current over 100 A, not to incur in overheating. During operation, we
 123 operated an air and water cooling system on the magnets and we remotely monitored
 124 the magnet temperatures.

₁₂₅ **0.2.2 Multi-Wire Proportional Chambers**

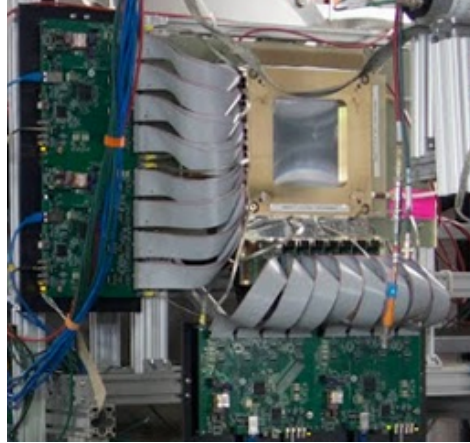


Figure 4: One of the four Multi Wire Proportional Chambers (WC) used in the LArIAT tertiary beamline and related read-out electronics.

₁₂₆ LArIAT uses four multi-wire proportional chambers, or wire chambers (WC) for
₁₂₇ short, two upstream and two downstream from the bending magnets. The geometry
₁₂₈ of one chamber is shown in Figure 4: the WC effective aperture is a square of 12.8 cm
₁₂₉ perpendicular to the beam direction. Inside the chamber, the 128 horizontal and 128
₁₃₀ vertical wires strung at a distance of 1 mm from each other in a mixture of 85% Argon
₁₃₁ and 15% isobutane gas. The WC operating voltage is between 2400 V and 2500 V.
₁₃₂ The LArIAT wire chambers are an upgraded version of the Fenker Chambers [11],
₁₃₃ where an extra grounding improves the signal to noise ratio of the electronic readout.

₁₃₄ Two ASDQ chips [14] mounted on a mother board plugged into the chamber serve
₁₃₅ as front end amplifier/discriminator. The chips are connected to a multi-hit TDC [13]
₁₃₆ which provides a fast OR output used as first level trigger. The TDC time resolution
₁₃₇ is 1.18 ns/bin and can accept 2 edges per 9 ns. The maximum event rate acceptable
₁₃₈ by the chamber system is 1 MHz: this rate is not a limiting factor considering that
₁₃₉ the rate of the tertiary particle beam at the first wire chamber is estimated to be less
₁₄₀ than 15 kHz. A full spill of data occurring once per supercycle is stored on the TDC
₁₄₁ board memory at once and read out by a specially designed controller. We use LVDS
₁₄₂ cables to carry both power and data between the controller and the TDCs and from

₁₄₃ the controller to the rest of the DAQ.

₁₄₄ Multi-Wire Proportional Chambers functionality

₁₄₅ We use the wire chamber system together with the bending magnets to measure the
₁₄₆ particle's momentum.

₁₄₇ In the simplest scenario, only one hit on each and every of the four wire chambers
₁₄₈ is recorded during a single readout of the detector systems. Thus, we use the hit
₁₄₉ positions in the two wire chambers upstream of the magnets to form a trajectory
₁₅₀ before the bend, and the hit positions in the two wire chambers downstream of the
₁₅₁ magnets to form a trajectory after the bend. We use the angles in the XZ plane
₁₅₂ between the upstream and downstream trajectories to calculate the Z component of
₁₅₃ the momentum as follows:

$$P_z = \frac{B_{eff}L_{eff}}{3.3(\sin(\theta_{DS}) - \sin(\theta_{US}))}, \quad (1)$$

₁₅₄ where B_{eff} is the effective maximum field in a square field approximation, L_{eff}
₁₅₅ is the effective length of both magnets (twice the effective length of one magnet),
₁₅₆ θ_{US} is the angle off the z axis of the upstream trajectory, θ_{DS} is the angle off the
₁₅₇ z axis of the downstream trajectory and $3.3 c^{-1}$ is the conversion factor from [T·m]
₁₅₈ to [MeV/c]. By using the hit positions on the third and fourth wire chamber, we
₁₅₉ estimate the azimuthal and polar angles of the particle trajectory, and we are able to
₁₆₀ calculate the other components of the momentum.

₁₆₁ The presence of multiple hits in a single wire chamber or the absence of hits in one
₁₆₂ (or more) wire chambers can complicate this simple scenario. The first complication
₁₆₃ is due to beam pile up, while the latter is due to wire chamber inefficiency. In the
₁₆₄ case of multiple hits on a single WC, at most one wire chamber track is reconstructed
₁₆₅ per event. Since the magnets bend particles only in the X direction, we assume
₁₆₆ the particle trajectory to be roughly constant in the YZ plane, thus we keep the

167 combination of hits which fit best with a straight line. It is still possible to reconstruct
168 the particle’s momentum even if the information is missing in either of the two middle
169 wire chambers (WC2 or WC3), by constraining the particle trajectory to cross the
170 plane in between the magnets.

171 Events satisfying the simplest scenario of one single hit in each of the four wire
172 chambers form the “Picky Track” sample. We construct another, higher statistics
173 sample, where we loosen the requirements on single hit and wire chamber efficiency:
174 the “High Yield” sample. For LArIAT Run II, the High Yield sample is about three
175 times the Picky Tracks statistics. For the first measurements of the LArIAT hadronic
176 cross section, we use the Picky Tracks sample because the uncertainty on the momen-
177 tum is smaller and the comparison with the beamline MC results is straightforward
178 compared with the High Yield sample; a possible future update and cross check of
179 these analysis would be the use of the High Yield sample.

180 **Four point track momentum uncertainty**

181 **0.2.3 Time-of-Flight System**

182 Two scintillator paddles, one upstream of the first set of WCs and one downstream
183 of the second set of WCs form LArIAT time-of-flight (TOF) detector system.

184 The upstream paddle is made of a 10 x 6 x 1 cm scintillator piece, read out by
185 two PMTs mounted on the beam left side which collect the light from light guides
186 mounted on all four edges of the scintillator. The downstream paddle is a 14 x 14 x
187 1 cm scintillator piece read out by two PMTs on the opposite ends of the scintillator,
188 as shown in figure 5. The relatively thin width in the beamline direction minimizes
189 energy loss of beam particles traveling through the scintillator material.

190 The CAEN 1751 digitizer is used to digitize the TOF PMTs signals at a sampling
191 rate of 1 GHz. The 12 bit samples are stored in a circular memory buffer. At trigger
192 time, data from the TOF PMTs are recorded to output in a 28.7 μ s windows starting

193 approximately 8.4 μ s before the trigger time.

194 **TOF functionality**

195 The TOF signals rise time (10-90%) is 4 ns and a full width, half-maximum of 9 ns
196 consistent in time. The signal amplitudes from the upstream TOF and downstream
197 TOF are slightly different: 200 mV for the upstream PMTs but only 50 mV for
198 downstream PMTs. The time of the pulses was calculated utilizing an oversampled
199 template derived from the data itself. We take the pulse pedestal from samples
200 far from the pulse and subtract it from the pulse amplitude. We then vertically
201 stretch a template to match the pedestal-subtracted pulse amplitude and we move
202 it horizontally to find the time. With this technique, we find a pulse time-pickoff
203 resolution better than 100 ps. The pulse pile up is not a significant problem given
204 the TOF timing resolution and the rate of the particle beam. Leveraging on the
205 pulses width uniformity of any given PMT, we flag events where two pulses overlap
206 as closely in time as 4 ns with a 90% efficiency according to simulation.

207 We combine the pulses from the two PMTs on each paddle to determine the
208 particles' arrival time by averaging the time measured from the single PMT, so to
209 minimize errors due to optical path differences in the scintillator. However, a time
210 spread of approximately 300 ps is present in both the upstream and downstream
211 detectors, likely due to transit time jitter in the PMTs themselves.

212 **0.2.4 Punch-Through and Muon Range Stack Instruments**

213 The punch-through and the muon range stack (MuRS) detectors are located down-
214 stream of the TPC. These detectors provide a sample of TPC crossing tracks without
215 relying on TPC information and can be used to improve particle ID for muons and
216 pions with momentum higher than 450 MeV/c.

217 The punch-through is simple sheet of scintillator material, read out by two PMTs.



Figure 5: Image of the down stream time of flight paddle, PMTs and relative support structure before mounting.

218 The MuRS is a segmented block of steel with four slots instrumented with scintillation
219 bars. The four steel layers in front of each instrumented slot are 2 cm, 2 cm, 14 cm
220 and 16 cm deep in the beam direction. Each instrumented slot is equipped with
221 four scintillation bars each, positioned horizontally in the direction orthogonal to the
222 beam. Each scintillator bar measures $\textcolor{red}{? \times ? \times 2}$ cm and it is read out by one PMT.

223 The signals from both the punch-thorough and the MuRS PMTs are sent to a
224 NIM discriminator. If the signal crosses the discriminator threshold, it is digitized in
225 the CAEN V1740, same as the TPC. The sampling time of the CAEN V1740 is slow
226 (of the order of 128 ns) and that the pulse shape information from the PMT is lost.
227 A Punch-thorough and MuRS signal will then be simply a “hit” at a given time in
228 the beamline event.

229 It is worth mentioning here the presence of an additional scintillation paddle
230 between WC4 and the downstream paddle of the TOF system, called halo. The
231 halo is a $39 \times 38 \times 1$ cm 3 paddle with a 6.5 cm radius hole in the center, whose original
232 function was to reject beam particles slightly offset from the beamline center. Data

233 from this paddle turned out to be unusable, so our data events include both particle
234 going through the halo scintillation material or through the halo hole.

235 0.2.5 LArIAT Cosmic Ray Paddle Detectors

236 LArIAT triggers both on beam events and on cosmic rays events. We perform this
237 latter trigger by using two sets of cosmic ray paddle detectors (a.k.a. “cosmic towers”.)
238 The cosmic towers frame the LArIAT cryostat, as one sits in the downstream left
239 corner and the other sits in the upstream right corner of the cryostat. Two paddle
240 sets of four scintillators pieces each make up each cosmic tower, an upper set and a
241 lower set per tower. Of the four paddles, a couple of two matched paddles stands
242 upright while the a second matched pair lies across the top of the assembly in the top
243 sets (or across the bottom of the assembly in the bottom sets). The horizontal couple
244 is used as a veto for particles traveling from inside the TPC out. The four signals
245 from the vertical paddles along one of the body diagonals of the TPC are combined
246 in a logical “AND”. This allows to select track due to cosmic muons at the ground
247 level crossing the TPC along one of its diagonals. Cosmic ray muons whose average
248 energy is in the few GeV range crossing both anode and cathode populate the events
249 triggered this way. This particularly useful sample of tracks is associated can be used
250 for many tasks; for example, we use anode-cathode piercing tracks to cross check
251 the TPC electric field on data (see Appendix A), to calibrate the charge response of
252 the TPC wires for the full TPC volume and to measure the electron lifetime in the
253 chamber [15].

254 We retrieved the scintillation paddles from the decommissioning of the CDF de-
255 tector at Fermilab and we used only the paddles with a counting efficiency greater
256 than 95% and low noise at working voltage. The measured trigger rate of the whole
257 system is 0.032 Hz, corresponding to ~ 2 muons per minute.



Figure 6: Photograph of one of the scintillation counters used in the cosmic towers.

258 0.3 In the Cryostat

259 0.3.1 Cryogenics and Argon Purity

260 LArIAT repurposed the ArgoNeuT cryostat [2] in order to use it in a beam of charged
261 particles, and added a new process piping and a new liquid argon filtration system in
262 FTBF. Inside the LArIAT experimental hall, the cryostat sits in the beam of charged
263 particles with its horizontal main axis oriented parallel to the secondary beam, 3°
264 off axis from the tertiary beam

265 Two volumes make up LArIAT cryostat, shown in Figure 7: the inner vessel and
266 the outer vessel. Purified liquid argon fills the inner vessel, while the outer volume
267 provides insulation through a vacuum jacket equipped with layers of aluminized mylar
268 superinsulation. The inner vessel is a cylinder of 130 cm length and 76.2 cm diameter,
269 containing about 550 L of LAr, corresponding to a mass of 0.77 ton. We run the signal
270 cables for the LArTPC and the high voltage feedthrough through a “chimney” at the
271 top and mid-length of the cryostat.

272 Given the different scopes of the ArgoNeuT and LArIAT detectors, we made
273 several modifications to the ArgoNeuT cryostat in order to use it in LArIAT. In
274 particular, the modifications shown in Figure 8 were necessary to account for the
275 beam of charged particles entering the TPC and to employ the new FTBF liquid

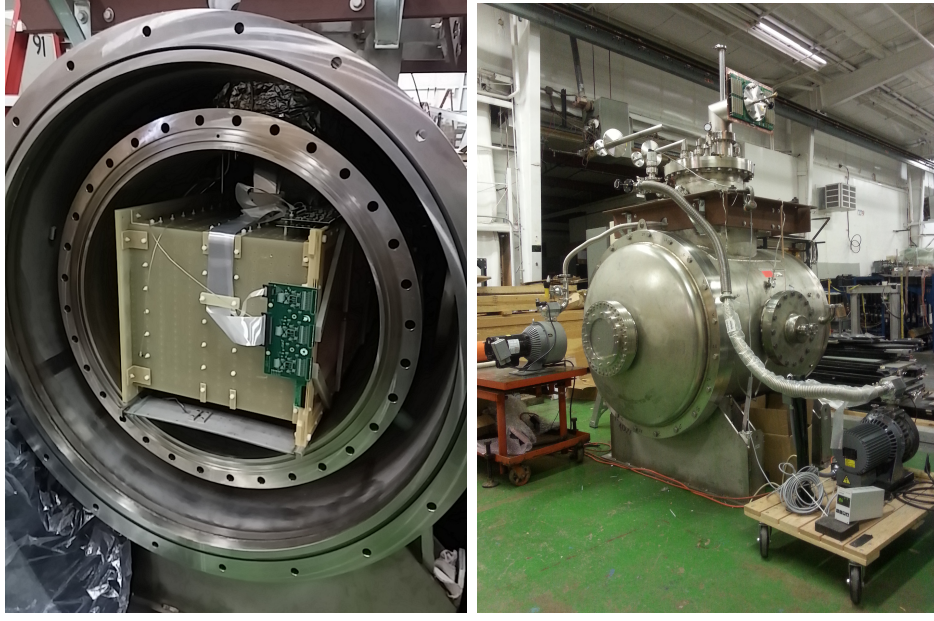


Figure 7: Left: the LArIAT TPC in the inner volume of the open cryostat. Right: cryostat fully sealed ready to be transported to FTBF.

276 argon purification system. We added a “beam window” on the front outer end cap
 277 and an “excluder” on the inner endcap, with the purpose of minimizing the amount of
 278 non-instrumented material upstream of the TPC’s active volume. The amount of non-
 279 instrumented material in front of the TPC for LArIAT corresponds to ~ 0.3 electron
 280 radiation lengths (X_0), to compare against the $\sim 1.6X_0$ of ArgoNeuT. To allow studies
 281 of the scintillation light, we added a side port feedthrough which enables the mounting
 282 of the light collection system, as well as the connections for the corresponding signal
 283 and high-voltage cables (see Section 0.3.3). We modified the bottom of the cryostat
 284 adding Conflat and ISO flange sealing to connect the liquid argon transfer line to the
 285 new argon cooling and purification system.

286 As in any other LArTPC, argon purity is a crucial parameter for LArIAT. Indeed,
 287 the presence of contaminants affects both the basic working principles of a LArTPC,
 288 as shown in section ???: electronegative contaminants such as oxygen and water de-
 289 crease the number of ionization electrons collected on the wires after drifting through
 290 the volume. In addition, contaminants such as Nitrogen decrease the light yield



Figure 8: Main modifications to the ArgoNeuT cryostat: 1) outlet for connection to the purification system at the bottom of the cryostat; 2) the “beam-window” on the outer endcap and “excluder” which reduces the amount of non-instrumented material before the TPC; 3) the side port to host the light collection system.

from scintillation light, especially in its slow component. In LArIAT, contaminations should not exceed the level of 0.2 parts per billion (ppb). We achieve this level of purity in several stages. The specifics required for the commercial argon bought for LArIAT are 2 parts per million (ppm) oxygen, 3.5 ppm water, and 10 ppm nitrogen. This argon is monitored with the use of commercial gas analyzer. Argon is stored in a dewar external to LArIAT hall and filtered before filling the TPC. LArIAT uses a filtration system designed for the Liquid Argon Purity Demonstrator (LAPD) [9]: half of a 77 liter filter contains a 4A molecular sieve (Sigma-Aldrich [16]) able to remove mainly water, while the other half contains BASF CU-0226 S, a highly dispersed copper oxide impregnated on a high surface area alumina, apt to remove mainly oxygen [4]. A single pass of argon in the filter is sufficient to achieve the necessary purity, unless the filter is saturated. In case the filter saturates, the media needs to be regenerated by using heated gas; this happened twice during the Run II period¹. The

¹ We deemed the filter regeneration necessary every time the electron lifetime dropped under 100 μ s.

304 electron lifetime during the full LArIAT data taking are shown in Figure ???. The
305 filtered argon reaches the inner vessel via a liquid feedthrough which is routed to the
306 bottom of the cryostat. Argon is not recirculated in the system; rather, it boils off and
307 vents to the atmosphere. During data taking, we replenish the argon in the cryostat
308 every 6 hours to keep the TPC high voltage feedthrough and cold electronics always
309 submerged. In fact, we constantly monitor the level, temperature, and pressure of
310 the argon both in the commercial dewar and inside the cryostat during data taking.

311 **0.3.2 LArTPC: Charge Collection**

312 The LArIAT Liquid Argon Time Projection Chamber is a rectangular box of dimen-
313 sions 47 cm (drift) x 40 cm (height) x 90 cm (length), containing 170 liters of Liquid
314 Argon. The LArTPC three major subcomponents are

- 315 1) the cathode and field cage,
- 316 2) the wire planes,
- 317 3) the read-out electronics.

318 **Cathode and field cage**

319 A G10 plain sheet with copper metallization on one of the 40 x 90 cm inner surfaces
320 forms the cathode. A high-voltage feedthrough on the top of the LArIAT cryostat
321 delivers the high voltage to the cathode; the purpose of the high voltage system
322 (Figure 9) is to drift ionization electrons from the interaction of charged particles
323 in the liquid argon to the wire planes. The power supply used in this system is a
324 Glassman LX125N16 [12] capable of generating up to -125 kV and 16 mA of current,
325 but operated at -23.5kV during LArIAT Run-II. The power supply is connected via
326 high voltage cables to a series of filter pots before finally reaching the cathode.

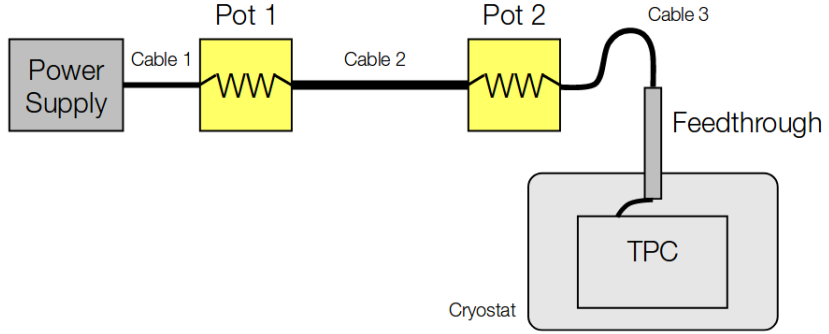


Figure 9: Schematic of the LArIAT high voltage system.

327 The field cage is made of twenty-three parallel copper rings framing the inner walls
 328 of the G10 TPC structure. A network of voltage-dividing resistors connected to the
 329 field cage rings steps down the high voltage from the cathode to form a uniform electric
 330 field. The electric field over the entire TPC drift volume is 486 V/cm, as measured
 331 in appendix A. The maximum drift length, i.e. the distance between cathode and
 332 anode planes, is 47 cm.

333 **Wire planes**

334 LArIAT Run-II has three wire planes separated by 4 mm spaces: in order of increasing
 335 distance from the cathode, they are the shield, the induction and the collection plane.
 336 The “wire pitch”, i.e., the distance between two adjacent wires in a given plane, is
 337 4 mm. The shield plane counts 225 parallel wires of equal length oriented vertically.
 338 This plane is not connected with the read-out electronics; rather it shields the outer
 339 planes from extremely long induction signals due to the ionization in the whole drift
 340 volume. As the shield plane acts almost like a Faraday cage, the resulting shape of
 341 signals in the first instrumented plane (induction) is easier to reconstruct. Both the
 342 induction and collection planes count 240 parallel wires of different length oriented at
 343 60° from the vertical with opposite signs. Electrons moving past the induction plane
 344 will induce a bipolar pulse on its wires; the drifting electrons will be then collected

³⁴⁵ on the collection plane's wires, forming a unipolar pulse.

³⁴⁶ The three wire planes and the cathode form three drift volumes, as shown in Figure
³⁴⁷ 10. The main drift volume is defined as the region between the cathode plane and the
³⁴⁸ shield plane (C-S). The other two drift regions are those between the shield plane and
³⁴⁹ the induction plane (S-I), and between the induction plane and the collection plane
³⁵⁰ (I-C). The electric field in these regions is chosen to satisfy the charge transparency
³⁵¹ condition and allow for 100% transmission of the drifting electrons through the shield
³⁵² and the induction planes.

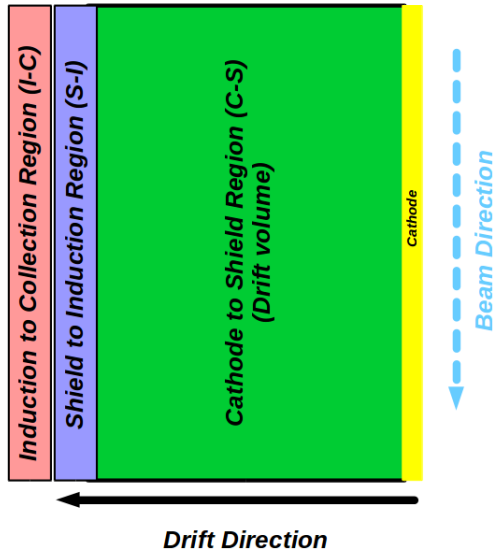


Figure 10: Schematic of the three drift regions inside the LArIAT TPC: the main drift volume between the cathode and the shield plane (C-S) in green, the region between the shield plane and the induction plane (S-I) in purple, and the region between the induction plane and the collection plane (I-C) in pink.

³⁵³ Table 1 provides the default voltages applied to the cathode and the shield, in-
³⁵⁴ duction, and collection plane.

Table 1: Cathode and anode planes default voltages

Cathode	Shield	Induction	Collection
-23.17 kV	-298.8 V	-18.5 V	338.5 V

355 **Electronics**

356 Dedicated electronics read the induction and collection plane wires, for a total of
357 480-channel analog signal path from the TPC wires to the signal digitizers. A digital
358 control system for the TPC-mounted electronics, a power supply, and a distribution
359 system complete the front-end system. Figure 11 shows a block diagram of the overall
360 system. The direct readout of the ionization electrons in liquid argon forms typically
361 small signals on the wires, which need amplification in oder to be processed. LArIAT
362 performs the amplification stage directly in cold with amplifiers mounted on the TPC
363 frame inside the liquid argon. The BNL ASICs adopted in LArIAT are designated as
364 LArASIC, version 4-star and are the same used by the MicroBooNE experiment [10].
365 The signal from the ASICs are driven to the other end of the readout chain, to the
366 CAEN V1740 digitizers [6]. The CAEN V1740 has a 12 bit resolution and a maximum
367 input range of 2 VDC, resulting in about 180 ADC count for a crossing MIP.

368 **0.3.3 LArTPC: Light Collection System**

369 The collection of scintillation photons is the second mechanism of particle detection
370 in argon other than the ionization electrons. Over the course of LArIAT’s three years
371 of data taking, the light collection system changed several times. We describe here
372 the light collection system for Run II. Two PMTs, a 3-inch diameter Hamamatsu
373 R-11065 and 2-inch diameter ETL D757KFL [1], as well as three SiPMs arrays (two
374 Hamamatsu S11828-3344M 4x4 arrays and one single-channel SensL MicroFB-60035)
375 are mounted on the PEEK support structure. PEEK screws into an access flange as
376 shown in Figure 12, on the anode side, leaving approximately 5 cm of clearance from
377 the collection plane.

378 Liquid argon scintillates in vacuum-ultraviolet (VUV) range at 128 nm; since
379 cryogenic PMTs are not sensitive to VUV wavelengths, we need to shift the light to a
380 range that is visible to the PMTs. In LArIAT, the wavelength shifting is achieved by

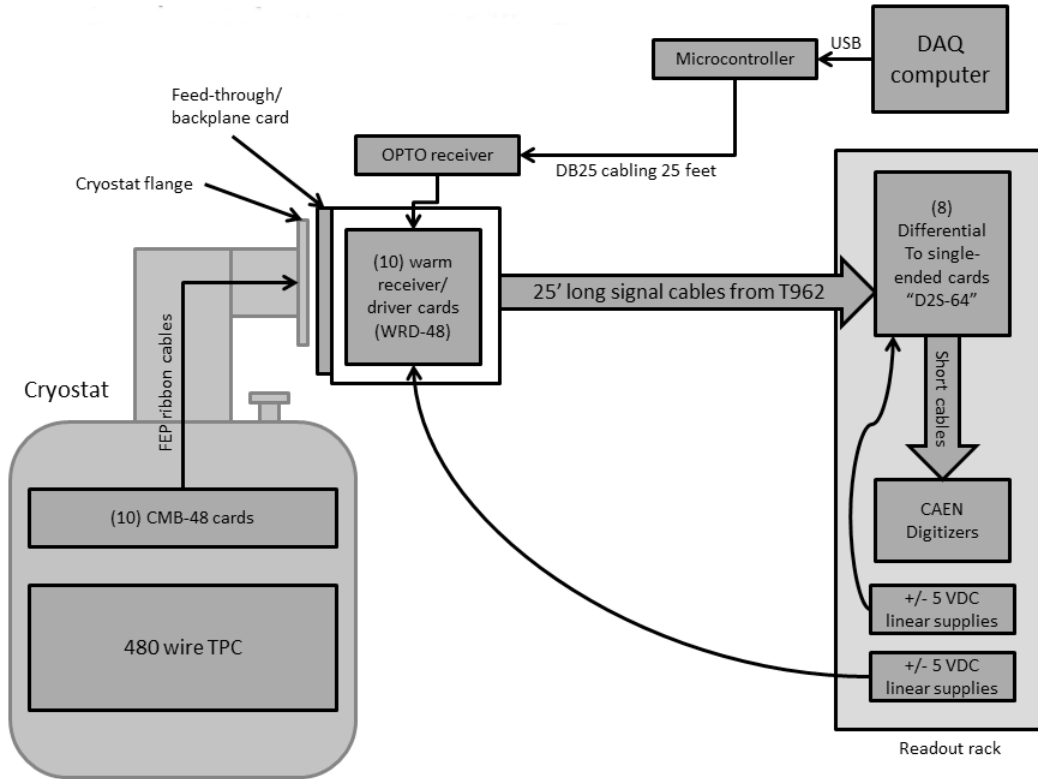


Figure 11: Overview of LArIAT Front End electronics.

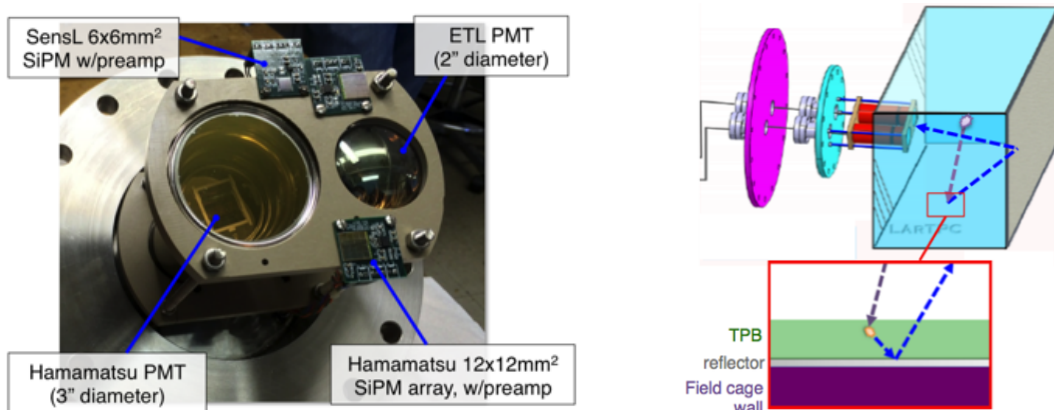


Figure 12: LArIAT's photodetector system for observing LAr scintillation light inside the TPC (left), and a simplified schematic of VUV light being wavelength-shifting along the TPB-coated reflecting foils (right).

381 installing highly-reflective 3M VIKUITI dielectric substrate foils coated with a thin
382 layer of tetraphenyl-butadiene (TPB) on the four unbiased walls of the TPC. The
383 scintillation light interaction with the TPB emits one or more visible photons, which
384 are then reflected into the chamber. Thus, the light yield increases and results in
385 higher uniformity of light across the TPC active volume, allowing the possibility of
386 light-based calorimetry, currently under study.

387 For Run II, we coated the windows of the ETL PMT and the SensL SiPM with
388 a thin layer of TPB. In doing so, some of the VUV scintillation light converts into
389 visible right at the sensor faces, keeping information on the direction of the light
390 source. Information about the light directionality is hindered for the light reflected
391 on foils, as the reflection is uniform in angle.

392 0.4 Trigger and DAQ

393 The LArIAT DAQ and trigger system governs the read out of all the many subsystems
394 forming LArIAT. The CAEN V1495 module [5] and its user-programmable FPGA are
395 the core of this system. Every 10 ns, this module checks for matches between sixteen
396 logical inputs and user-defined patterns in the trigger menu; if it finds a match for
397 two consecutive clock ticks, that trigger fires.

398 LArIAT receives three logic signals from the Fermilab accelerator complex related
399 to the beam timing which we use as input triggers: a pulse just before the beam, a
400 pulse indicating beam-on, and a beam-off pulse.

401 The beam instruments, the cosmic ray taggers, and the light collection system
402 provide the other NIM-standard logic pulse inputs to the trigger decision. We auto-
403 matically log the trigger inputs configuration with the rest of the DAQ configuration
404 at the beginning of each run.

405 Fundamental inputs to the trigger card come from the TOF (see section 0.2.3)

406 and the wire chambers (see section 0.2.2), as activity in these systems points to the
407 presence of a charged particle in tertiary beam line. In particular, the discriminated
408 pulses from the TOF PMTs form a NIM logic pulse for the trigger logic. We ask
409 for a coincidence within a 20 ns window for all the pulses from the PMTs looking at
410 the same scintillator block and use a delayed coincidence between the upstream and
411 downstream paddle to inform the trigger decision. In order to form a coincidence
412 between the upstream and downstream paddles, we delay the upstream paddle coin-
413 cidence by 20 ns and widen it by 100 ns. The delay and widening are necessary to
414 account for both lightspeed particles and slower particles (high-mass) to travel the
415 6.5 m between the upstream and the downstream paddles. For the read out of the
416 wire chambers, we use a total of sixteen multi-hit TDCs [13], four per chamber: two
417 TDC per plane (horizontal and vertical), sixty-four wires per TDC. In each TDC, we
418 keep the logical “OR” for any signal over threshold from the sixty-four wires. We
419 then require a coincidence between the “OR” for the horizontal TDCs and the “OR”
420 for the vertical TDCs: with this logic we make sure that at least one horizontal wire
421 and one vertical wire saw significant signal in one wire chamber. The single logical
422 pulse from each of the four wire chambers feeds into the first four inputs to the V1495
423 trigger card. We require a coincidence within 20 ns of at least three logical inputs to
424 form a trigger.

425 The cosmic towers (see Section 0.2.5) provide another primary input to the trigger,
426 in order to capture long tracks from cosmic muons crossing the TPC. We use NIM
427 modules to require coincidences between one upper and one lower paddle set of any
428 opposite cosmic towers. The OR all the opposite towers’ coincidences is fed as an
429 input to the trigger card.

430 We use the signal from the cryogenic PMTs (see Section 0.3.3) to form several
431 interesting triggers. The coincidence of signals from all the PMT pulses within \sim 20 ns
432 is an indication of ionizing radiation in the TPC and forms a trigger input. The

433 coincidence of two subsequent scintillation logic pulses delayed by a maximum of 7 μ s
434 forms the Michel electron trigger.

435 0.5 Control Systems

436 LArIAT is a complex ensemble of systems which needed to be monitored simultaneously during data taking. We performed the monitoring of the systems operations with a slow control system, a DAQ monitoring system and a low level data quality monitoring described in the following sections.

440 Slow Control

441 We used the Synoptic Java Web Start framework [3] as a real-time display of subsystem conditions. Its simple Synoptic provides a Graphical User Interface that talks to the Fermilab Accelerator Control System via the ACNET protocol. Graphical User Interface allowed us to change the operating parameters and to graph the trends of several variables of interest for all of the tertiary beam detectors. Among the most important quantities monitored by Synoptic there are the level of argon in both the inner vessel and the external dewar, the operating voltages of cathode and wire planes, of the PMTs and SiPMs, and of the four wire chambers, as well as the magnets temperature. Figure 13 shows an example of the monitoring system. LArIAT uses the Accelerator Control NETwork system (ACNET) to monitor the beam conditions of the MCenter beamline. For example, the horizontal and vertical position of the beam at the first two wire chambers (WC1 and WC2) are shown in 14 as seen by the shifter during data taking.

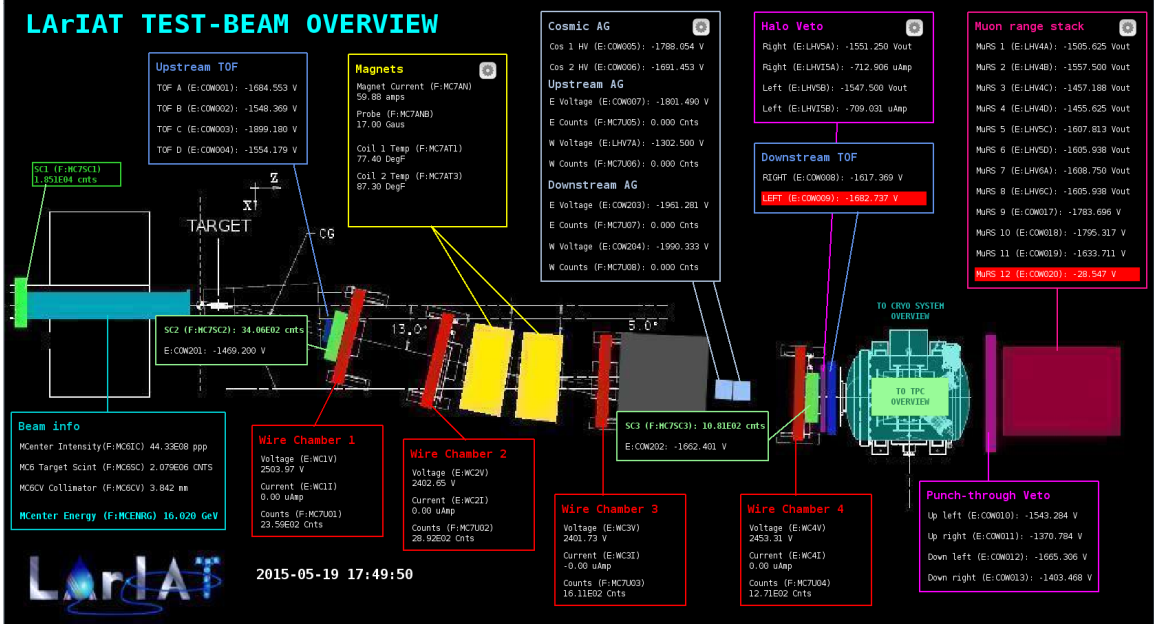


Figure 13: Interface of the Synoptic slow control system

454 DAQ Monitoring

455 We monitor the data taking and the run time evolution with the Run Status Webpage
 456 (<http://lariat-wbm.fnal.gov/lariat/run.html>), a webpage updated in real-time. The
 457 page displays, among other information, the total number of triggers in the event,
 458 the total number of detectors triggered during a beam spill, the trigger patterns, the
 459 number of times a particular trigger pattern was satisfied during a beam spill, and
 460 the current time relative to the Fermilab accelerator complex supercycle. A screen
 461 shot of the page is show in figure 15.

462 Data Quality Monitoring

463 We employ two systems to ensure the quality of our data during data taking: the
 464 Near-Real-Time Data Quality Monitoring and the Event Viewer.

465 The Near-Real-Time Data Quality Monitoring (DQM) is a webpage which receives
 466 updates from all the VME boards in the trigger system and displays the results of
 467 a quick analysis of the DAQ stream of raw data on a spill-by-spill basis. The DQM

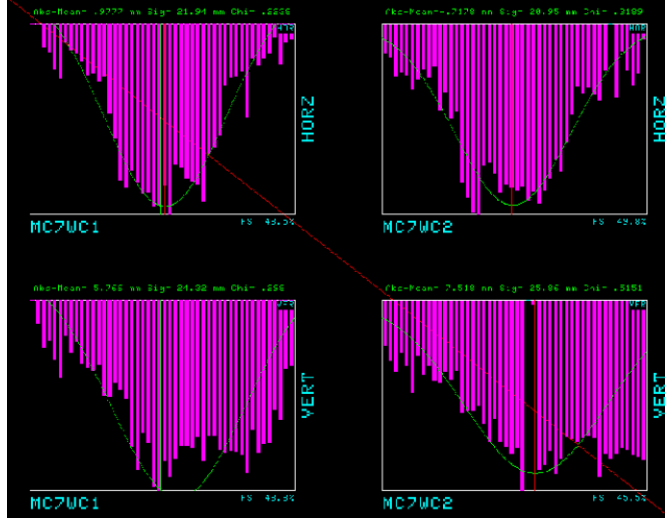


Figure 14: Beam position at the upstream wire chambers monitored with ACNET.

468 allows the shifter to monitor almost in real time (typically with a 2-minute delay)
 469 a series of low level-quantities and compare them to past collections of beam spills.
 470 Some of the variables monitored in the DQM are the pedestal mean and RMS on
 471 CAEN digitizer boards of the TPC wires and PMTs of the beamline detectors, the
 472 hit occupancy and timing plots on the wire chambers, and number of data fragments
 473 recorded that are used to build a TPC event. Abnormal values for low-level quantity
 474 in the data activate a series of alarms in the DQM; this quick feedback on the DAQ
 475 and beam conditions is fundamental to assure a fast debugging of the detector and a
 476 very efficient data taking during beam uptime.

477 The online Event Viewer displays a two dimensional representation (Wire vs Time)
 478 of LArIAT TPC events on both the Induction and the Collection planes in near real
 479 time. The raw pulses collected by the DAQ on each wire are plotted as a function of
 480 drift time, resulting in an image of the TPC event easily readable by the shifter. This
 481 tool guarantees a particularly good check of the TPC operation which activate an
 482 immediate feedback for troubleshooting a number of issues. For example, it is easy for
 483 the shifter to spot high occupancy events and request a reduction of the primary beam
 484 intensity, or to spot a decrease of the argon purity which requires the regeneration of

⁴⁸⁵ filters, or to catch the presence of electronic noise and reboot the ASICs. An example
⁴⁸⁶ of high occupancy event is shown in 16.

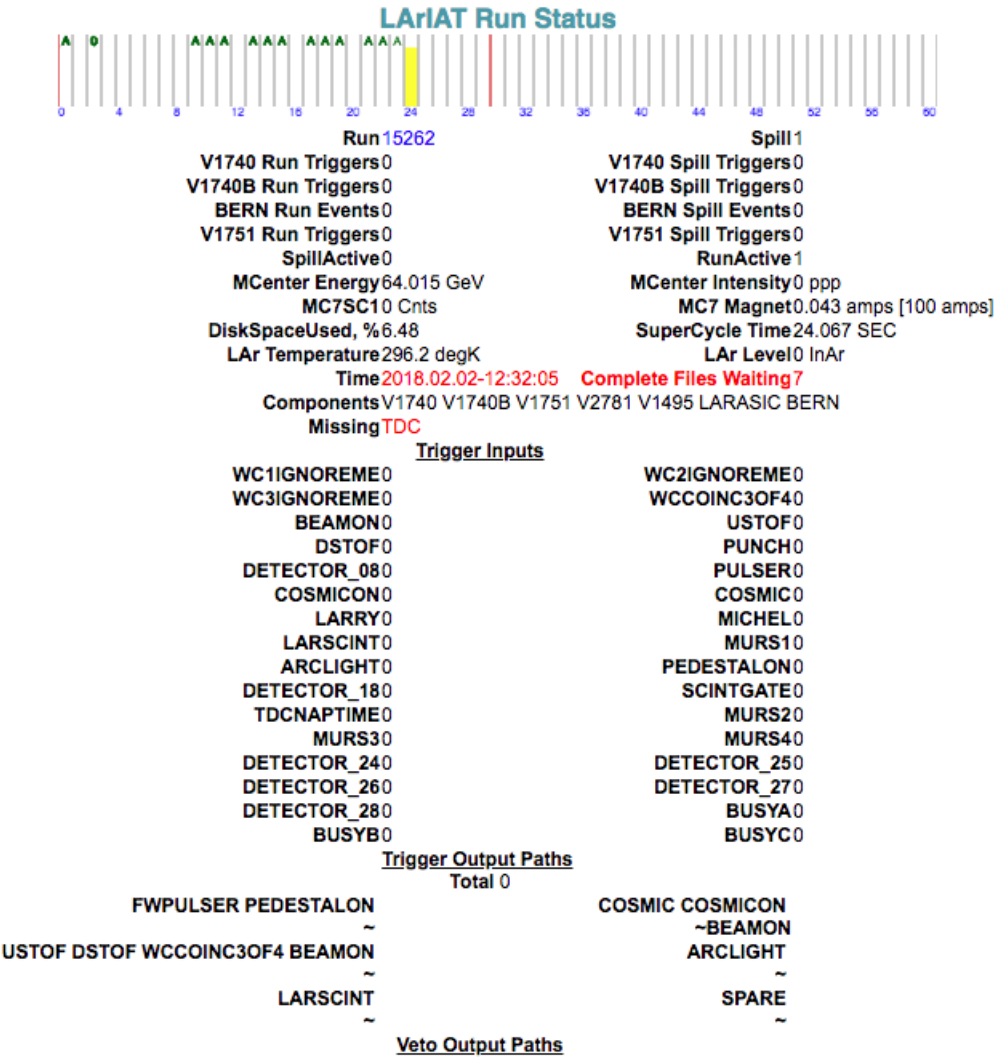


Figure 15: Run Status page at LArIAT downtime. At the top the yellow bar displays the current position in the Fermilab supercycle. Interesting information to be monitored by the shifter were the run number and number of spills, time elapsed from data taking (here in red), the energy of the secondary beam and the trigger paths.

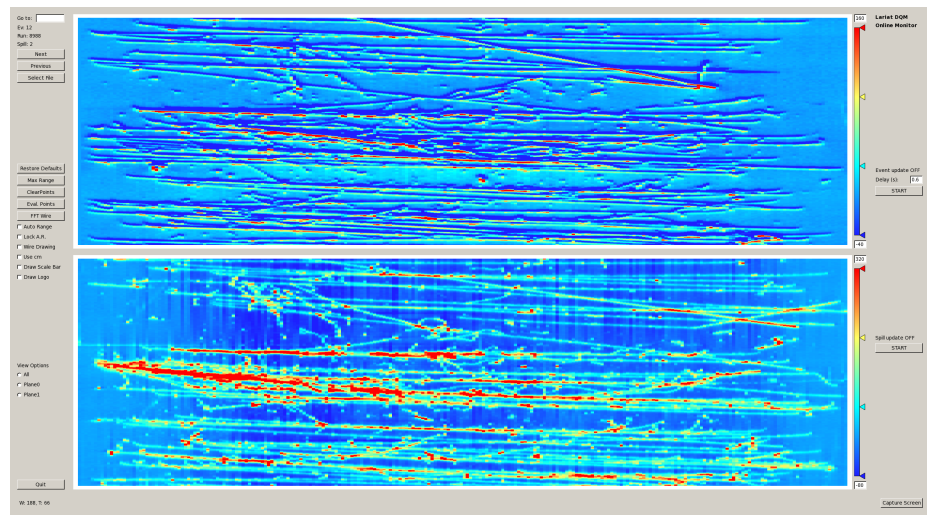


Figure 16: High occupancy event display: induction plane (top) and collection plane (bottom).

⁴⁸⁷ **Appendix A**

⁴⁸⁸ **Measurement of LArIAT Electric**
⁴⁸⁹ **Field**

⁴⁹⁰ The electric field of a LArTPC in the drift volume is a fundamental quantity for
⁴⁹¹ the proper functionality of this technology, as it affects almost every reconstructed
⁴⁹² quantity such as the position of hits or their collected charge. Given its importance,
⁴⁹³ we calculate the electric field for LArIAT with a single line diagram from our HV
⁴⁹⁴ circuit and we cross check the obtained value with a measurement relying only on
⁴⁹⁵ TPC data.

⁴⁹⁶ Before getting into the details of the measurement procedures, it is important to
⁴⁹⁷ explicit the relationship between some quantities in play. The electric field and the
⁴⁹⁸ drift velocity (v_{drift}) are related as follows

$$v_{drift} = \mu(E_{field}, T)E_{field}, \quad (\text{A.1})$$

⁴⁹⁹ where μ is the electron mobility, which depends on the electric field and on the
⁵⁰⁰ temperature (T). The empirical formula for this dependency is described in [?] and
⁵⁰¹ shown in Figure A.1 for several argon temperatures.

⁵⁰² The relationship between the drift time (t_{drift}) and the drift velocity is trivially

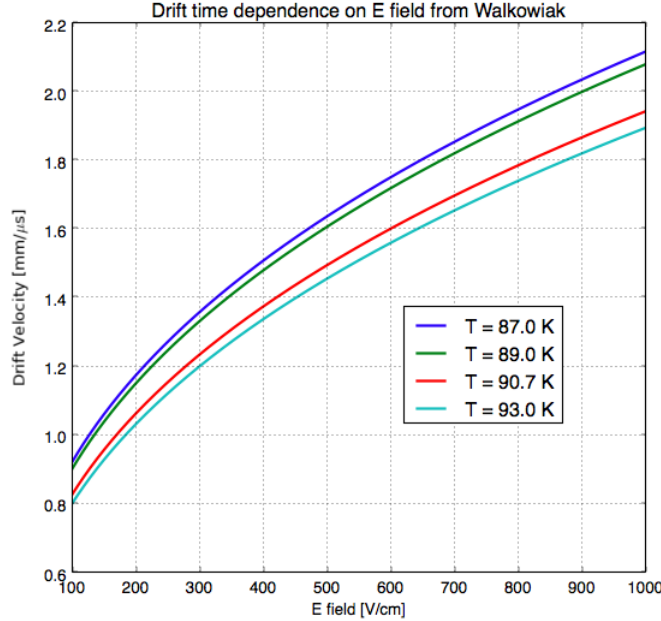


Figure A.1: Drift velocity dependence on electric field for several temperatures. The slope of the line at any one point represents the electron mobility for that given temperature and electric field.

Table A.1: Electric field and drift velocities in LArIAT smaller drift volumes

	Shield-Induction	Induction-Collection
E_{filed}	700.625 V/cm	892.5 V/cm
v_{drift}	1.73 mm/μs	1.90 mm/μs
t_{drift}	2.31 μs	2.11 μs

503 given by

$$t_{drift} = \Delta x / v_{drift}, \quad (\text{A.2})$$

504 where Δx is the distance between the edges of the drift region. Table A.1 reports the

505 values of the electric field, drift velocity, and drift times for the smaller drift volumes.

506 With these basic parameters established, we can now move on to calculating the

507 electric field in the main drift region (between the cathode and the shield plane).

508 Single line diagram method

509 The electric field strength in the LArIAT main drift volume can be determined know-
 510 ing the voltage applied to the cathode, the voltage applied at the shield plane, and the
 511 distance between them. We assume the distance between the cathode and the shield
 512 plane to be 470 mm and any length contraction due to the liquid argon is negligibly
 513 small (~ 2 mm).

514 The voltage applied to the cathode can be calculated using Ohm's law and the
 515 single line diagram shown in Figure A.2. A set of two filter pots for emergency power
 516 dissipation are positioned between the Glassman power supply and the cathode, one at
 517 each end of the feeder cable, each with an internal resistance of $40 \text{ M}\Omega$. The output
 518 current of the Glassman power supply is then used to determine the electric field
 519 strength. Figure A.3 shows an average current of 0.004172 mA from the Glassman
 520 power supply.

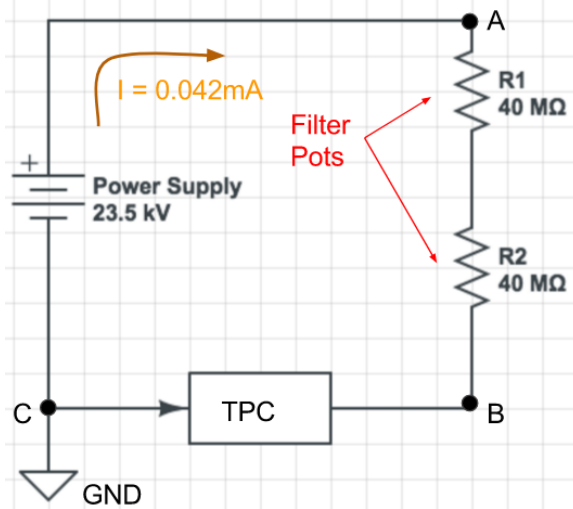


Figure A.2: get rid of current line LAr-IAT HV simple schematics.

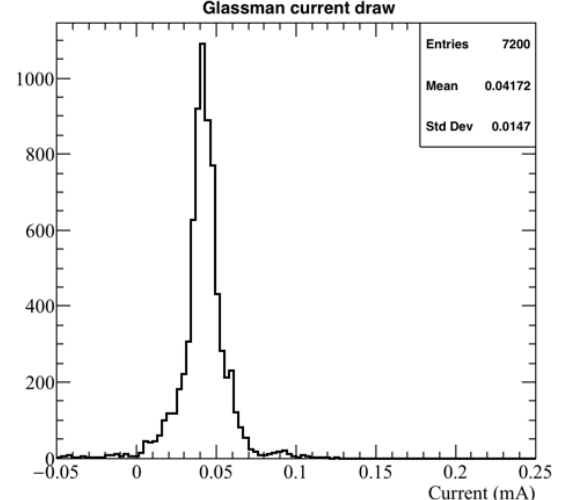


Figure A.3: **the axis is wrong!!** Current reading from the Glassman between May 25th and May 30th, 2016 (typical Run-II conditions).

521 Using this current, the voltage at the cathode is calculated as

$$V_{BC} = V_{PS} - (I \times R_{eq}) = -23.5 \text{ kV} + (0.00417 \text{ mA} \times 80 \text{ M}\Omega) = -23.17 \text{ kV}, \quad (\text{A.3})$$

522 where I is the current and R_{eq} is the equivalent resistor representing the two filter
523 pots. The electric field, drift voltage, and drift time are then calculated to be

$$E_{\text{field}} = \frac{V_{BC} - V_{\text{shield}}}{\Delta x} = 486.54 \text{ V/cm} \quad (\text{A.4})$$

524 **E field using cathode-anode piercing tracks**

525 We devise an independent method to measure the drift time (and consequently drift
526 velocity and electric field) using TPC cathode to anode piercing tracks. We use this
527 method as a cross check to the single line method. The basic idea is simple:

- 528 0. Select cosmic ray events with only 1 reconstructed track
- 529 1. Reduce the events to the one containing tracks that cross both anode and
530 cathode
- 531 2. Identify the first and last hit of the track
- 532 3. Measure the time difference between these two hits (Δt).

533 This method works under the assumptions that the time it takes for a cosmic particle
534 to cross the chamber ($\sim \text{ns}$) is small compared to the charge drift time (\sim hundreds
535 of μs).

536 We choose cosmic events to allow for a high number of anode to cathode piercing
537 tracks (ACP tracks), rejecting beam events where the particles travel almost perpen-
538 dicularly to drift direction. We select events with only one reconstructed track to
539 maximize the chance of selecting a single crossing muon (no-michel electron). We
540 utilize ACP tracks because their hits span the full drift length of the TPC, see figure

541 A.4, allowing us to define where the first and last hit of the tracks are located in space
542 regardless of our assumption of the electric field.

543 One of the main features of this method is that it doesn't rely on the measurement
544 of the trigger time. Since Δt is the time difference between the first and last hit of a
545 track and we assume the charge started drifting at the same time for both hits, the
546 measurement of the absolute beginning of drift time t_0 is unnecessary. We boost the
547 presence of ACP tracks in the cosmic sample by imposing the following requirements
548 on tracks:

- 549 • vertical position (Y) of first and last hits within ± 18 cm from TPC center
550 (avoid Top-Bottom tracks)
- 551 • horizontal position (Z) of first and last hits within 2 and 86 cm from TPC front
552 face (avoid through going tracks)
- 553 • track length greater than 48 cm (more likely to be crossing)
- 554 • angle from the drift direction (phi in figure A.5) smaller than 50 deg (more
555 reliable tracking)
- 556 • angle from the beam direction (theta in figure A.5) grater than 50 deg (more
557 reliable tracking)

558 Tracks passing all these selection requirements are used for the Δt calculation.

559 For each track passing our selection, we loop through the associated hits in order
560 to retrieve the timing information. The analysis is performed separately on hits on the
561 collection plane and induction plane, but lead to consistent results. As an example
562 of the time difference, figures A.6 and A.7 represent the difference in time between
563 the last and first hit of the selected tracks for Run-II Positive Polarity sample on the
564 collection and induction plane respectively. We fit with a Gaussian to the peak of the
565 Δt distributions to extract the mean drift time and the uncertainty associated with

566 it. The long tail at low Δt represent contamination of non-ACP tracks in the track
 567 selection. We apply the same procedure to Run-I and Run-II, positive and negative
 568 polarity alike.

569 To convert Δt recorded for the hits on the induction plane to the drift time we
 570 utilize the formula

$$t_{drift} = \Delta t - t_{S-I} \quad (\text{A.5})$$

571 where t_{drift} is the time the charge takes to drift in the main volume between the
 572 cathode and the shield plane and t_{S-I} is the time it takes for the charge to drift from
 573 the shield plane to the induction plane. In Table A.1 we calculated the drift velocity
 574 in the S-I region, thus we can calculate t_{S-I} as

$$t_{S-I} = \frac{l_{S-I}}{v_{S-I}} = \frac{4mm}{1.745mm/\mu s} \quad (\text{A.6})$$

575 where l_{S-I} is the distance between the shield and induction plane and v_{S-I} is the drift
 576 velocity in the same region. A completely analogous procedure is followed for the hits
 577 on the collection plane, taking into account the time the charge spent in drifting from
 578 shield to induction as well as between the induction and collection plane. The value
 579 for Δt_{drift} , the calculated drift velocity (v_{drift}), and corresponding drift electric field
 580 for the various run periods is given in Table A.2 and are consistent with the electric
 581 field value calculated with the single line diagram method.

Delta t_{drift} , drift v and E field with ACP tracks

Data Period	Δt_{Drift} [μs]	Drift velocity [mm/ μs]	E field [V/cm]
RunI Positive Polarity Induction	311.1 ± 2.4	1.51 ± 0.01	486.6 ± 21
RunI Positive Polarity Collection	310.9 ± 2.6	1.51 ± 0.01	487.2 ± 21
RunII Positive Polarity Induction	315.7 ± 2.8	1.49 ± 0.01	467.9 ± 21
RunII Positive Polarity Collection	315.7 ± 2.7	1.49 ± 0.01	467.9 ± 21
RunII Negative Polarity Induction	315.9 ± 2.6	1.49 ± 0.01	467.1 ± 21
RunII Negative Polarity Collection	315.1 ± 2.8	1.49 ± 0.01	470.3 ± 21
Average Values	314.1	1.50 ± 0.01	474.3 ± 21

Table A.2: Δt for the different data samples used for the Anode-Cathode Piercing tracks study.

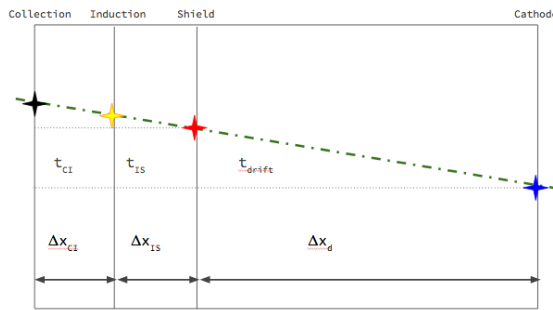


Figure A.4: Pictorial representation of the YX view of the TPC. The distance within the anode planes and between the shield plane and the cathode is purposely out of proportion to illustrate the time difference between hits on collection and induction. A ACP track is shown as an example.

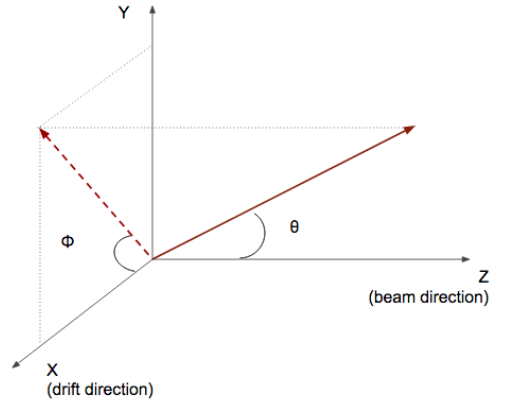


Figure A.5: Angle definition in the context of LArIAT coordinates system.

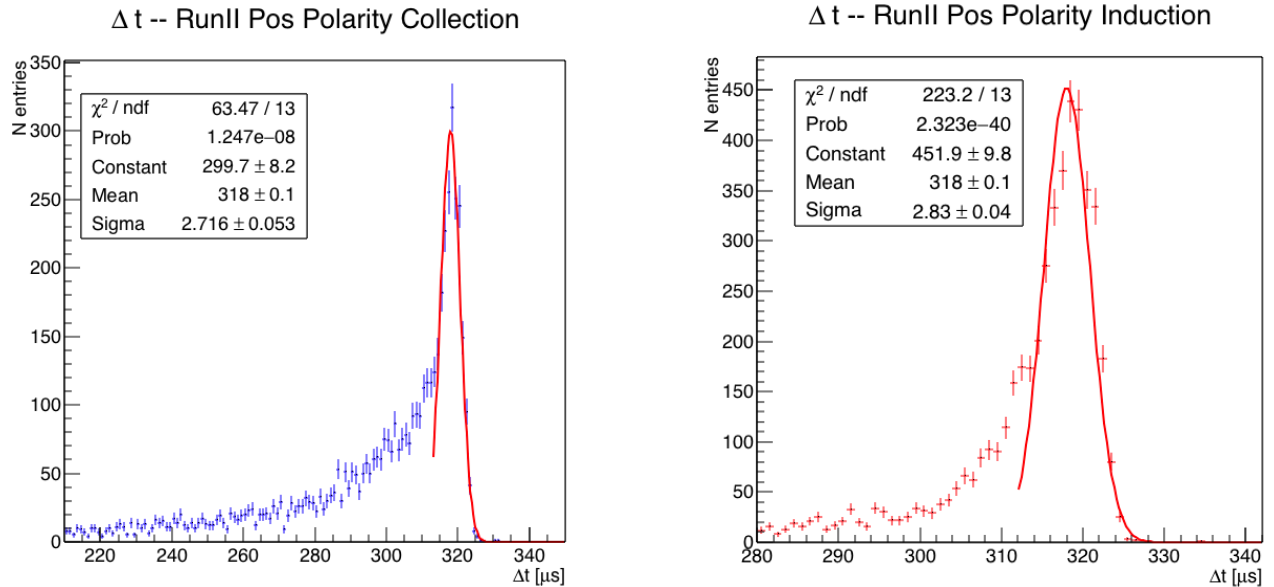


Figure A.6: Collection plane Δt fit for Run II positive polarity ACP data selected tracks.

Figure A.7: Induction plane Δt fit for Run II positive polarity ACP data selected tracks.

582 **Bibliography**

- 583 [1] R. Acciarri et al. Demonstration and Comparison of Operation of Photomulti-
584 plier Tubes at Liquid Argon Temperature. *JINST*, 7:P01016, 2012.
- 585 [2] C. Anderson et al. The ArgoNeuT Detector in the NuMI Low-Energy beam line
586 at Fermilab. *JINST*, 7:P10019, 2012.
- 587 [3] Timofei Bolshakov Andrey Petrov. Java synoptic toolkit. Technical report, Sept
588 2010.
- 589 [4] BASF Corp. 100 Park Avenue, Florham Park, NJ 07932 USA.
- 590 [5] CAEN. Caen v1495 data sheet. Technical report, jan 2018.
- 591 [6] CAEN. Caen v1740 data sheet. Technical report, jan 2018.
- 592 [7] The LArIAT Collaboration. The liquid argon in a testbeam (lariat) experiment.
593 Technical report, In Preparation 2018.
- 594 [8] L. Aliaga et al. Minerva neutrino detector response measured with test beam
595 data. *Nuclear Instruments and Methods in Physics Research Section A: Acceler-
596 ators, Spectrometers, Detectors and Associated Equipment*, 789:28 – 42, 2015.
- 597 [9] M Adamowski et al. The liquid argon purity demonstrator. *Journal of Instru-
598 mentation*, 9(07):P07005, 2014.

- 599 [10] R. Acciarri et al. Design and construction of the MicroBooNE detector. *Journal*
600 *of Instrumentation*, 12(02):P02017–P02017, feb 2017.
- 601 [11] H Fenker. Standard beam pwc for fermilab. Technical report, Fermi National
602 Accelerator Lab., Batavia, IL (USA), 1983.
- 603 [12] Glassman High Voltage, Inc., Precision Regulated High Voltage DC Power Sup-
604 ply.
- 605 [13] S. Hansen, D. Jensen, G. Savage, E. Skup, and A. Soha. Fermilab test beam
606 multi-wire proportional chamber tracking system upgrade. June 2014. Interna-
607 tional Conference on Technology and Instrumentation in Particle Physics (TIPP
608 2014).
- 609 [14] FM Newcomer, S Tedja, R Van Berg, J Van der Spiegel, and HH Williams.
610 A fast, low power, amplifier-shaper-discriminator for high rate straw tracking
611 systems. *IEEE Transactions on Nuclear Science*, 40(4):630–636, 1993.
- 612 [15] T. Yang R. Acciarri, M. Stancari. Determination of the electron lifetime in lariat.
613 Technical report, March 2016.
- 614 [16] Sigma-Aldrich, P.O. Box 14508, St. Louis, MO 63178 USA.